

# Diagnostic Imaging and Radiology in Physiotherapy



# Diagnostic Imaging and Radiology in Physiotherapy

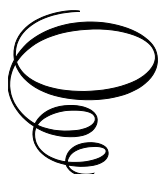
Edited by

Dominik Sieron

Editors of the English Edition

Andreas Christe and Johannes Heverhagen

**Cambridge  
Scholars  
Publishing**



Diagnostic Imaging and Radiology in Physiotherapy

Edited by Dominik Sieroń

Editors of the English Edition  
Andreas Christe and Johannes Heverhagen

This book first published 2020

Cambridge Scholars Publishing

Lady Stephenson Library, Newcastle upon Tyne, NE6 2PA, UK

British Library Cataloguing in Publication Data  
A catalogue record for this book is available from the British Library

Copyright © 2020 by Dominik Sieroń, Andreas Christe,  
Johannes Heverhagen and contributors

All rights for this book reserved. No part of this book may be reproduced, stored in a retrieval system, or transmitted, in any form or by any means, electronic, mechanical, photocopying, recording or otherwise, without the prior permission of the copyright owner.

ISBN (10): 1-5275-3753-6

ISBN (13): 978-1-5275-3753-8

# CONTENTS

List of Figures.....	vii
Author Affiliations .....	xvi
Chapter One.....	1
Introduction to diagnostic imaging (radiology) in physiotherapy Dominik Sieroń, Andreas Christe, Wadim Wojciechowski, Johannes Heverhagen	
Chapter Two .....	6
Brain imaging Jerzy Walecki, Dominik Sieroń, Wadim Wojciechowski,	
Chapter Three .....	21
Imaging of the cervical spine Dominik Sieroń, Andreas Christe, Marek Tombarkiewicz, Johannes Heverhagen	
Chapter Four.....	41
Imaging of the thoracic and lumbosacral spine Dominik Sieroń, Andreas Christe, Daniel Knap, Johannes Heverhagen	
Chapter Five .....	81
Imaging of the shoulder girdle Dominik Sieron, Andreas Christe, Natalia Orlecka, Johannes Heverhagen	
Chapter Six.....	114
Imaging of the elbow joint Dominik Sieroń, Andreas Christe, Maciej Honkowicz, Daniel Knap, Johannes Heverhagen	
Chapter Seven.....	132
Imaging of the arm, forearm and wrist Maciej Honkowicz, Dominik Sieroń, Andreas Christe, Johannes Heverhagen	

Chapter Eight.....	157
Imaging of the pelvis and hip joint	
Dominik Sieroń, Andreas Christe, Przemysław Kaczmarek, Johannes Heverhagen	
Chapter Nine.....	171
Imaging of the knee joint	
Dominik Sieroń, Andreas Christe, Lukasz Mazurek, Johannes Heverhagen	
Chapter Ten .....	206
Imaging of the ankle joint and tarsal bones	
Dominik Sieroń, Andreas Christe, Maciej Honkowicz, Daniel Knap, Johannes Heverhagen	
Chapter Eleven .....	232
Prostheses and implants in diagnostic imaging of the musculoskeletal system	
Dominik Sieroń, Andreas Christe, Adam Sulewski, Johannes Heverhagen	

## LIST OF FIGURES

- Figure 2.1. A) Normal brain on sagittal CT image. B) Normal brain on transverse CT image after contrast application.
- Figure 2.2. Normal brain vessels visible on angio-CT after 3D reconstruction in the sagittal plane.
- Figure 2.3. Chronic subdural hematoma after road accident visible on transverse CT image.
- Figure 2.4. Subdural hematoma (arrow) with mass effect visible on CT in the transverse plane (asterisk). Parts of the hematoma is hypodense indicating also old hemorrhage.
- Figure 2.5. Subarachnoid hemorrhage due to a ruptured aneurysm (arrow), blood also entered into the lateral ventricle (asterisk).
- Figure 2.6. Ischemic changes in the subacute phase in the right occipital lobe (asterisk) observed on MRI with the fluid-attenuated inversion recovery sequence in the transverse plane.
- Figure 2.7. Acute stroke visible on transverse MR image in a) ADC and b) DWI. DWI and ADC sequence reveals diffusion restriction in ischemic lesion (asterisk), left side which is typical for acute phase of the disease.
- Figure 2.8. Transverse sinus thrombosis: a) thrombosis on the right side visible on transverse CT image (black arrow); b) thrombus on the right side visible on MR with the T1-weighted sequence in the transverse plane after the intravenous administration of a contrast agent (white arrow).
- Figure 2.9. MIP (Maximum intensity projection) MRI reconstruction showing transverse sinus thrombosis on the right (arrow).
- Figure 2.10. Venous malformation/hemangioma in the left cerebellar hemisphere visible on CT in the transverse plane (asterisk).
- Figure 2.11. Ischemic changes in the acute phase on diffusion-weighted imaging MR sequence in the transverse plane (asterisk).
- Figure 2.12. Multiple Sclerosis: Typical finger shaped lesions adjacent to the ventricle (asterisk) on the sagittal MR sequence.
- Figure 2.13. A) Diffuse leukodegenerative changes at the level of semiovale centers visible on the transverse FLAIR sequence (asterisk). B) Symmetrical, medium degree atrophy of the brain visible on the T2-weighted sequences without dementia and other neurological deficits.
- Figure 2.14. Demyelinating (arrow) and atrophic changes (asterisk) in the brain visible on the transverse fluid-attenuated inversion recovery sequence.
- Figure 2.15. Enhanced cortico-subcortical atrophy of the brain within the temporal (arrow) and frontal lobes visible on the transverse MRI fluid-attenuated inversion recovery sequence.

- Figure 2.16. Transverse MRI: brain tumor originating from the quadrigeminal plate: a) with the T1-weighted sequence after the intravenous administration of a contrast agent (asterisk); b) with the magnetization transfer contrast MRI sequence after the administration of the contrast agent (asterisk).
- Figure 2.17. Glioma is visible in left thalamic glioma on the transverse MR image T2-weighted sequence. Tumor slightly pressing on structures of midbrain.
- Figure 3.1. T2-weighted images of the normal cervical spine in the a) sagittal plane and b) axial plane.
- Figure 3.2. Cervical image obtained by X-ray lateral projection. Visible absent physiological lordosis decreased intervertebral space between level C5/C6.
- Figures 3.3. a), b). Functional cervical X-ray in the lateral projection: a - in the anteflexion; b - in the retroflexion. The anteflexion shows forward displacement of the upper compared to the lower adjacent vertebral body from C2 to C6. The vertebral arrangement is aligned in retroflexion.
- Figure 3.4. Thoracic image obtained by X-ray anterior-posterior projection with visible minor degenerative changes.
- Figure 3.5. Degenerative and proliferative changes of end plates of vertebral bodies and intervertebral joints on X-ray in a lateral projection (arrow).
- Figure 3.6. Proliferative changes at vertebral body edges and multilevel reduction of intervertebral spaces of the cervical spine on X-rays in an anterior-posterior projection.
- Figure 3.7. Fracture of the uncinat process of cervical spine on the right of the body of C6 vertebrae visible on X-ray in an anterior-posterior projection.
- Figure 3.8. Advanced degenerative-proliferative changes of vertebral bodies (arrow) with coexisting multilevel decrease of intervertebral spaces of the cervical spine (asterisks) visible on CT in sagittal plane.
- Figure 3.9. C2 vertebrae and dens axis fracture visible on anterior-posterior on X-ray projection through the open mouth (arrow).
- Figure 3.10. Old fracture of dens axis (arrow) visible in a sagittal plane on CT imagine.
- Figure 3.11: An anterior C2 vertebral arch fracture (arrow) seen on both sides on a CT scan in the transverse plane.
- Figure 3.12. A fracture of the posterior arch of C2 vertebrae (arrow) visible on both sides of the CT transverse plane.
- Figure 3.13: MR of the cervical spine displays discopathy: a - in the transverse plane at the level of vertebrae bodies C5-C6 (arrow).; b - hemangiomas of the vertebral bodies C6 and C7 are visible in the sagittal plane (arrow).
- Figure 3.14. Cervical spine discopathy at the level of C5/C6 with a noticeable narrowing of the prevertebral fluid space in the sagittal plane.
- Figure 3.15. Wide-based herniation of the intervertebral disc shallows fluid space and lateral recesses, compressing the nerve roots. T2 weighted MR sequence: a - in the transverse plane (arrow); b – T2 weighted sequence with fat saturation in the sagittal plane (arrow).
- Fig. 3.16. Multilevel discopathy of the cervical spine, exacerbated on the levels C3/C4 to C6/C7 with spinal cord compression in the sagittal plane.

- Figure 3.17. MRI-Myelography of the normal cervical spine as seen in the coronal plane.
- Figure 3.18: Modelling of the cervical spinal cord and shallowing of intervertebral foramen on both sides, left more than right (arrow), visible on the MR image in the transverse plane.
- Figure 4.1. Scheuermann's disease with degenerative changes visible on CT scan in the sagittal plane: typical Schmorl's nodes are marked with arrows.
- Figure 4.2. Posttraumatic compression fracture of the superior vertebral end plate of L4 visible on CT in sagittal plane.
- Figure 4.3. Pathological changes related to cancerous processes and compression fracture of T12 with destruction (arrow) visible on CT in the sagittal plane.
- Figure 4.4. Posttraumatic impression fracture of T4 and T5 in the area of the superior vertebra end plate with reduced vertebral height on the sagittal MRI (arrows).
- Figure 4.5. Spondylolisthesis of L3 and L4 (arrow) visible on MRI in the sagittal plane: a) degenerative changes in the vertebral bodies (arrows); b) status after transpedicular stabilization.
- Figure 4.6. Anterior spondylolisthesis of L4/L5 visible on CT in the sagittal plane (arrow).
- Figure 4.7. Central posterior protrusion of the intervertebral disc (asterisk) causing compression of the dural sac, shallowing of the lateral processes and bilateral nerve root compression (arrow).
- Figure 4.8. Massive posterior intervertebral disc herniation (arrow) with damage to the fibrous ring and prolapse of the nucleus pulposus at the level of L5–S1 on sagittal MRI.
- Figure 4.9. Scheuermann's disease and degenerative fracture of the superior vertebral end plate of L3 visible on MRI in the sagittal plane (asterisks).
- Figure 4.10. T2-weighted transverse MRI of the spine: broad-based posterior intervertebral disc protrusion at L5/S1 (asterisk) causing nerve root compression on both sides, but more on the right side (arrow).
- Figure 4.11. The right-sided intervertebral disc herniation (asterisk) causing shallowing of the lateral recesses and pressure on the nerve root on the right side (arrow) visible on MRI in the transverse plane.
- Figure 4.12. Multilevel discopathy with degeneration of vertebral bodies and intervertebral discs of the lumbosacral spine visible on MRI in the sagittal plane (arrows).
- Figure 4.13. Multilevel degenerative changes in the vertebral bodies and intervertebral discs of the lumbosacral spine with anterior and posterior disc protrusions (arrows).
- Figure 4.14. Degenerative-proliferative changes with narrowing of the intervertebral spaces and scoliosis of the lumbosacral spine visible on X-ray examination in the anteroposterior projection.
- Figure 4.15. A small degree of leftward scoliosis of the thoracic/lumbar spine visible on X-ray examination in the anteroposterior projection.
- Figure 4.16. An example of rightwards scoliosis of the thoracic spine in a young patient with an immature skeletal system visible on X-ray examination in the anteroposterior projection.

- Figure 4.17. Interarticular degeneration of the facet joints of the thoracic and lumbar spine visible (arrows) on a sagittal CT image.
- Figure 4.18. Degenerative lesions of the L5/S1 intervertebral disc (asterisk) with discontinuity of the fibrous ring (arrow) visible on MRI in the sagittal plane.
- Figure 4.19. Left lumbar scoliosis with rotation of the vertebral bodies and degeneration of the vertebral end plates on X-ray examination in the anteroposterior projection.
- Figure 4.20. Post inflammatory and degenerative sclerotic changes at the level of L3/L4 (asterisks) with coexisting degenerative-proliferative lesions (arrows) visible on sagittal CT.
- Figure 4.21. Scheuermann's disease (arrow) with anterior wedging of T6 on MRI in the sagittal plane.
- Figure 4.22. Posttraumatic fracture of L4 with secondary narrowing of the spinal canal and modeling of the filum terminale visible on MRI in the a) transverse plane (asterisks) and b) sagittal plane (asterisk).
- Figure 4.23. a) Narrowing of the intervertebral space at level of L5/S1 (asterisk) and to a lesser extent at level of L4/L5 (arrow). b) Chronic degenerative changes in the lumbosacral spine with degeneration of the L3 and L4 vertebrae, narrowing of the intervertebral spaces of the L3–S1 segment and degenerative intervertebral changes (arrow), as well as advanced atherosclerosis of the aorta and iliac arteries.
- Figure 4.24. Bilateral inflammatory changes with great severity in the right sacroiliac joint (arrow) visible on coronal MRI.
- Figure 4.25. Another example of bilateral inflammatory sacroiliac joint lesions (arrows) visible on MRI in the coronal plane.
- Figure 4.26. Osteoporosis of the lumbosacral spine with fractures of L1 and L3 on X-ray examination: a) anteroposterior projection; b) lateral projection (asterisks).
- Figure 4.27. Vertical fracture of the sacrum (massa lateralis) based on osteoporotic changes (arrows) and pelvic phleboliths visible on CT after 3D reconstruction.
- Figure 4.28. Fracture of the upper end plate of L3 and vertebra plana of T12 (asterisks) based on osteoporotic changes visible on CT in the sagittal plane.
- Figure 4.29. Bilateral fractures of the sacrum (arrow and asterisks) based on osteoporotic changes observed on CT image in the coronal plane.
- Figure 5.1. Fracture of the lateral clavicle shaft with dislocation of the ends (arrow) visible on X-ray examination in the anteroposterior projection.
- Figure 5.2. Posttraumatic impairment of the acromio-clavicular joint (Rockwood type II) on MRI with the intra-articular administration of a contrast agent in the a) transverse plane (arrow) and b) coronal plane (asterisks).
- Figure 5.3. Fracture of the acromion with slight lateral displacement (arrow) on X-ray examination in the anteroposterior projection.
- Figure 5.4. CT image after 3D reconstruction: multiple fractures (asterisks) of the scapula.
- Figure 5.5. Anteroinferior fracture of the glenoid, referred to as a Bankart fracture (arrow), visible on CT after 3D reconstruction.
- Figure 5.6. Damage to the lower edge of the glenoid bony Bankart type (arrow) visible on X-ray examination.

- Figure 5.7. Anterior shoulder dislocation (asterisks) visible on X-ray examination.
- Figure 5.8. Hill-Sachs fracture of the humeral head (asterisks) visible on CT after 3D reconstruction.
- Figure 5.9. Inverted Hill-Sachs fracture (asterisk) visible on X-ray examination.
- Figure 5.10. Inverted Hill-Sachs fracture on MRI in the transverse plane with the intra-articular administration of a contrast agent (asterisk).
- Figure 5.11. Posterior shoulder dislocation (asterisks) can be missed on anteroposterior projection on X-ray examination.
- Figure 5.12. Posterior dislocation of the shoulder joint with extensive damage to the joint surface of the humeral head visible on X-ray examination in the axial projection.
- Figure 5.13. Total rupture of the supraspinatus tendon of the shoulder joint (arrow) visible on MRI on the coronal plane.
- Figure 5.14. Partial rupture of the supraspinatus tendon in the articular area visible on MRI in the coronal plane.
- Figure 5.15. Metallic artifacts of metal implants (arrow) after reconstruction of the rotator cuff visible on MRI on the transverse plane.
- Figure 5.16. Anterior dislocation of the right shoulder joint (asterisks) visible on X-ray examination on the anteroposterior projection.
- Figure 5.17. Bankart-type injury to the labrum visible on MRI on the transverse plane with the intra-articular administration of a contrast agent.
- Figure 5.18. SLAP type II injury of the labrum visible on MRI on the coronal plane with the intra-articular administration of a contrast agent.
- Figure 5.19. Arthrography of the shoulder joint is a basic examination for assessing the structure of the labrum.
- Figure 5.20. Buford recess (asterisks) is a normal anatomic variant visible on MRI in the transverse plane.
- Figure 5.21. Fluid in the tendon sheath of the long head of the biceps brachii (arrow) visible on transverse T2-weighted MRI.
- Figure 5.22. Advanced arthrosis of the acromioclavicular joint (arrow) visible on X-ray examination in the anteroposterior projection.
- Figure 5.23. Inflammatory changes in the acromioclavicular joint (arrow) with secondary joint degeneration visible on MRI in the coronal plane.
- Figure 5.24. Calcific deposits in the supraspinatus tendon (tendinitis calcarea) visible on X-ray examination in the anteroposterior projection.
- Figure 5.25. Degenerative changes in the acromioclavicular joint (arrow) with osteophyte (asterisk) visible on X-ray examination in the anteroposterior projection.
- Figure 5.26. Humeral head chondroma (arrow) visible on MRI in the sagittal plane after the administration of a contrast agent.
- Figure 5.27. Chondroma of the humeral neck (arrow) visible on MRI in the sagittal plane after the intra-articular administration of a contrast agent.
- Figure 6.1. Posttraumatic arthrosis of the elbow joint with compression fracture with cystic changes of the articular surface of the humeral trochlea (white arrow), osteophytes of the coracoid process (asterisk), and enthesopathy of the distal attachment of the triceps brachii (black arrow) visible on MRI.

- Figure 6.2. Comminuted fracture of the coronoid process (arrow) visible on CT in the transverse plane.
- Figure 6.3. Fracture of the coronoid process (arrow) visible on CT in the sagittal plane.
- Figure 6.4. Monteggia fracture visible on X-ray examination in the a) lateral (asterisk) and b) anteroposterior projections (arrow).
- Figure 6.5. Osteosynthesis of Monteggia fracture with coexisting radial fracture visible on X-ray examination on the anteroposterior projection.
- Figure 6.6. "Tennis elbow" visible on MRI in the coronal plane.
- Figure 6.7. Damage to the lateral collateral ligament (arrow) of the elbow joint visible on MRI in the coronal plane.
- Figure 6.8. Synovial osteochondromatosis observed on X-ray examination in the lateral projection (arrow).
- Figure 6.9. Degenerative changes in the elbow joint with osteophyte (arrow) visible on X-ray examination in the a) anteroposterior and b) lateral projections.
- Figure 6.10. Degenerative changes in the joint surface of the elbow with osteophytes (arrow) visible on CT after 3D reconstruction.
- Figure 7.1. Fracture of the distal radius (arrow) visible on X-ray examination in the a) anteroposterior and b) lateral projections.
- Figure 7.2. Colles' fracture (arrow) with joint surface impression (asterisk) visible on X-ray examination in the a) anteroposterior and b) lateral projections.
- Figure 7.3. Fracture of the styloid process (asterisk) and chronic posttraumatic free bone element (arrow) visible on X-ray examination in the lateral projection.
- Figure 7.4. Status after fracture of the distal ulna a) initially (arrow and asterisk) and b) after one month with callus formation (arrow and asterisk) on X-ray examination in the anteroposterior projection.
- Figure 7.5. A normal wrist on X-ray examination in a projection targeting the navicular bone.
- Figure 7.6. Damage to the triangular fibrocartilage complex (arrows) visible on MRI in the coronal plane.
- Figure 8.1. Normal hip joints on CT in the coronal plane.
- Figure 8.2. Bilateral degeneration of the hip joints (arrows) with phleboliths, i.e., calcifications within venous vessels (asterisk) in the pelvis, visible on X-ray examination in the anteroposterior projection.
- Figure 8.3. Degeneration of the hip joints with osteophytes (arrows) related to the femoroacetabular impingement visible on CT in the coronal plane.
- Figure 8.4. Bilateral cam-type FAI with pistol grip configuration (arrows) intensified on the right side visible on X-ray examination on the anteroposterior projection.
- Figure 8.5. Degenerative calcification (arrow) in the vicinity of the upper edge of the acetabulum visible on X-ray examination on the axial projection.
- Figure 8.6. Pincer-type FAI (arrows) visible on CT in the transverse plane.
- Figure 8.7. Posttraumatic superior labrum tear injury (arrow) of the hip joint visible on MRI in the coronal projection.
- Figure 8.8. Fresh damage to the articular labrum (arrow) of the hip joint without bony pathologies visible on MRI.

Figure 8.9. Damage to the articular labrum of the hip joint in the superior-posterior region with a paralabral cyst (arrow) visible on MRI in the transversal planes.

Figure 8.10. Right hip joint showing irregular anterior damage to the labrum on MR arthrography.

Figure 8.11. Hip joint fracture (asterisk) with posterior dislocation of the femoral head (arrow) in the left hip joint on CT image in the transverse plane.

Figure 8.12. Unhealed fracture of the left femoral head/shaft (arrows) with alleged joint formation visible on CT a) in the transverse plane, b) in the coronal plane, c) and after 3D reconstruction.

Figure 8.13. Hip endoprosthesis with paraprotetic hip fracture (arrow) visible on X-ray examination in the axial projection.

Figure 9.1. Example of the knee joint MR arthrography in the sagittal plane.

Figure 9.2. Traumatic wedge-shaped cavity within Hoffa's body (asterisk) in transverse MRI.

Figure 9.3. Condition after stabilization of a distal femoral shaft fracture with metallic artifacts (asterisk) visible on MRI on the transverse plane.

Figure 9.4. Impression fracture of the tibial plateau (arrows) and tibial metaphysis (asterisk) on CT in the coronal plane.

Figure 9.5. Burst fracture of the tibia visible on CT after 3D reconstruction, view from the top with multiple fracture lines (arrows and asterisk).

Figure 9.6. Orthopedic osteosynthesis (arrow) of a patellar bone fracture on a) MRI in the transverse plane with metal artifacts and b) X-ray examination in the lateral projection.

Figure 9.7. Posttraumatic damage to the patellar cartilage (arrow) visible on MRI in the transverse plane.

Figure 9.8. Degenerative damage to the medial part (arrow) of the patellar (asterisk) cartilage with coexisting cracks, an increased amount of fluid in the joint cavity, and thickening of the synovial membrane is visible on MRI in the transverse plane.

Figure 9.9. Medial fold syndrome (arrow) visible on MRI in the a) transverse and b) sagittal planes.

Figure 9.10. Damage to the medial meniscus (arrow) with coexisting femoral impression fracture and cartilage injury (asterisk) visible on MRI in the sagittal plane.

Figure 9.11. Fracture of the proximal tibia (arrow) visible on X-ray examination in the anteroposterior projection.

Figure 9.12. Bone infarction visible on MRI in the sagittal plane.

Figure 9.13. Multiple, complex cracks in the posterior-medial meniscus horn and an increased amount of fluid in the knee cavity visible on T2-weighted MRI in the sagittal plane.

Figure 9.14. Damage to the front horn of the medial meniscus visible as tear (arrow) on transverse MRI.

Figure 9.15. Injury of the medial collateral ligament (asterisk) on transverse MRI.

Figure 9.16. Rupture of the medial (tibial) collateral ligament (arrow) visible on MRI in the coronal plane.

- Figure 9.17. Pellegrini-Stieda lesion after damage to the proximal attachment of the tibial collateral ligament (arrow) visible on X-ray examination in the anteroposterior projection.
- Figure 9.18. Strain of the proximal attachment of the lateral collateral ligament (arrow) on coronal MRI.
- Figure 9.19. Sprain of the proximal attachment of the lateral collateral ligament (arrow) visible on MRI in the a) coronal and b) transverse planes.
- Figure 9.20. Rupture of the ACL with a characteristic imaging feature called the "empty notch sign" visible on MRI in the a) coronal (arrow) and b) sagittal planes (asterisk).
- Figure 9.21. Complete rupture of the ACL (arrow) on sagittal MRI.
- Figure 9.22. Complete rupture of the ACL (asterisk) visible on MRI in the sagittal plane.
- Figure 9.23. Posttraumatic and degenerative changes in the ACL with rupture (arrows) visible on MRI in the sagittal plane.
- Figure 9.24. Angular positioning of the PCL (asterisk) with intermediate features of ACL damage (arrows) visible on MRI in the sagittal plane.
- Figure 9.25. The double PCL sign (white and black arrow), where the lower band corresponds to a bucket handle tear of the meniscus lower arrow) visible on MRI in the sagittal plane.
- Figure 9.26. Damage to the PCL (arrow) visible on MRI in the a) sagittal and b) coronal planes.
- Figure 9.27. Compression fracture of the tibia with bone bruise (asterisk) visible on MRI in the coronal plane.
- Figure 9.28. Posttraumatic focal damage to the medial condylar cartilage of the femur with adjacent bone marrow edema (arrow) on sagittal MRI.
- Figure 10.1. Normal bone structures visible on CT after 3D reconstruction.
- Figure 10.2. Normal distal ankle joint ligaments visible on MRI in the coronal plane.
- Figure 10.3. a) Achilles tendinitis with hyperperfusion in the sagittal ultrasound image and b) secondary thickening on transverse ultrasound examination.
- Figure 10.4. Medial ankle fracture (arrows) visible on a) CT in the coronal plane and b) corresponding X-ray examination in the anteroposterior projection.
- Figure 10.5. Osteonecrosis of the calcaneus (arrows) visible on MRI in the a) sagittal and b) coronal planes.
- Figure 10.6. Calcaneal osteotomy (asterisk) with fixation (arrow) visible on X-ray examination a) in the lateral projection and b) in the projection targeting the calcaneus.
- Figure 10.7. Posttraumatic lipoma (asterisk) in the foot visible on CT in the sagittal plane.
- Figure 10.8. Status after consolidation of the navicular bone visible on CT in 3D.
- Figure 10.9. Diffuse osteopenia in the context of chronic immobilization of the foot (asterisk) and degenerative changes in the talonavicular joint (arrow). These tests also show upward subluxation of the navicular bone in the talonavicular joint. Images obtained by CT with the MPR method in the sagittal plane.

- Figure 10.10. Posttraumatic osteonecrosis of the talus with a free body fragment (arrow) conflicting with the tarsal sinus visible on CT in the sagittal plane.
- Figure 10.11. Post inflammatory damage to the tarsal canal (RA, arrow) visible on CT in the sagittal plane.
- Figure 10.12. Partial rupture of the Achilles tendon (arrow) visible on MRI in the transverse plane.
- Figure 10.13. Inflamed plantar aponeurosis (arrow) visible on MRI in the a) sagittal and b) coronal plane.
- Figure 10.14. Posttraumatic damage to the tibiofibular syndesmosis (asterisk) visible on MRI in the transverse plane.
- Figure 10.15. Rupture of the ankle joint capsule (arrow) visible on MRI in the sagittal plane.
- Figure 10.16. Damage to the anterior talofibular ligament (asterisk) and the joint capsule rupture (arrow) on MRI in the transverse plane.
- Figure 11.1. Condition after surgical stabilization of the cervical spine on X-ray examination in the a) anterolateral and b) lateral projections.
- Figure 11.2 a), b) Post vertebroplasty of thoracic vertebrae on X-ray examination in the lateral projection.
- Figure 11.3. Status after transpedicular stabilization of the lumbar spine on X-ray examination in the a) lateral and b) anteroposterior projections.
- Figure 11.4. Total anatomical right shoulder arthroplasty on X-ray examination in the anteroposterior projection.
- Figure 11.5. Inverted joint prosthesis of the shoulder on X-ray in the anteroposterior projection.
- Figure 11.6. Condition after orthopedic treatment of the labrum with surgical anchors visible on X-ray examination in the anteroposterior projection.
- Figure 11.7. Status after orthopedic stabilization of ulnar fracture visible on X-ray examination in the a) lateral and b) anteroposterior projections.
- Figure 11.8. Condition after total hip arthroplasty visible on X-ray examination in the anteroposterior projection.
- Figure 11.10. Stabilization of tibial plateau fracture and Pellegrini-Stieda damage (arrows) visible on X-ray examination in the anteroposterior projection.
- Figure 11.11. a), b) Status after surgical stabilization of lateral and medial ankle fractures visible on X-ray examination in the anteroposterior projections.
- Figure 11.12. Stabilization/ankylosis of the upper and lower ankle with screws.

## AUTHOR AFFILIATIONS

Dominik Sieron, MD, PhD, BC  
Institute of Radiology, Tiefenau Hospital, Inselgroup,  
University of Bern, Switzerland.

Prof. Andreas Christe, MD  
Department of Diagnostic, Interventional and Pediatric Radiology,  
Inselspital, Bern University Hospital, University of Bern, Switzerland.

Prof. Johannes T. Heverhagen, MD  
Department of Diagnostic, Interventional and Pediatric Radiology,  
Inselspital, Bern University Hospital, University of Bern, Switzerland.

Profesor Jerzy Walecki, MD  
Department of Radiology, Prof A. Gruca Independent Public Hospital,  
Center of Postgraduate Medical Education, Otwock, Poland

Prof. Philipp Wiggermann, MSc  
Department of Radiology and Nuclear Medicine,  
Hospital Braunschweig, Braunschweig, Germany.

Ivan Platzek, MD, PhD  
Dresden University Hospital  
Department of Radiology, Germany.

Wadim Wojciechowski, MD, PhD, Associate Professor.  
Department of Radiology,  
Jagiellonian University Medical College in Krakow, Poland.

Marek Tombarkiewicz, MD, PhD, MBA  
National Institute of Geriatrics, Rheumatology and Rehabilitation in  
Warsaw, Poland.

Daniel Knap, MD, PhD  
Leszek Giec Upper-Silesian Medical Center  
Silesian Medical University in Katowice, Poland.

Łukasz Mazurek, MD, PhD  
Private Diagnostic Center” Tomograf” in Tychy, Poland.

Adam Sulewski, MD, PhD  
Wiktor Dega's Orthopaedic and Rehabilitation Clinical Hospital,  
Poznan University of Medical Sciences, Poland.

Przemysław Kaczmarek, MD, PhD  
Private Outpatients and Diagnostic Center” OPTI-MED” in Nowy Sącz,  
Poland.

Natalia Orlecka, MD  
Leszek Giec Upper-Silesian Medical Center  
Silesian Medical University in Katowice, Poland.

Maciej Honkowicz, MD  
Leszek Giec Upper-Silesian Medical Center  
Silesian Medical University in Katowice, Poland.

Marcin Koroński, MD  
E. Szczeklik Specialist Hospital in Tarnów, Poland



# CHAPTER ONE

## INTRODUCTION TO DIAGNOSTIC IMAGING (RADIOLOGY) IN PHYSIOTHERAPY

Modern methods of radiology and diagnostic imaging allow excellent assessment of anatomical structures and pathological presentations throughout the human body. This specialization has a significant impact on patient therapy through increasing image quality. This book will present diagnostic methods used in everyday practice.

### **Radiography**

X-rays were discovered by Wilhelm Roentgen in 1895, and this discovery marked the beginning of a new specialization, i.e., radiology. Since the discovery of X-rays, many changes have been made in the development of X-ray testing technology, X-ray tube designs, X-ray films, recorders and cassettes.

Historically, X-ray images were obtained as a result of X-ray film irradiation by a beam of rays and differences in tissue absorption. X-ray images were created by X-rays colliding with special phosphor crystals in the screen placed in the cassette between the amplifying screens. When X-rays collide with phosphor crystals, light at specific wavelengths is absorbed and illuminates the film. This method, using amplifying screens, reduces the amount of radiation needed to take an X-ray and decreases the amount of radiation absorbed. This form of imaging is described as analog and is becoming less frequently used.

Currently, X-ray images are created in digital radiation devices, which allow the images to be saved to a variety of digital memory media. CDs or DVDs delivered to patients usually contain software for viewing the image data, which allows basic editing. Images can be enlarged or enhanced to represent selected structures to the desired extent. All these activities can be performed on any computer equipped with appropriate monitors for proper

display of the diagnostic images. Imaging tests can be stored in the archives using the PACS (picture archiving and communication system).

Before a typical X-ray procedure, the radiology technician places the patient in an appropriate position such that two or more planes of the selected body part can be imaged. The most frequently chosen projections include the anteroposterior (AP) and posteroanterior (PA) projections. Depending on the clinical needs, lateral or inclined projections can also be used. Selection of the projection depends on the location of changes and the clinical status of the patient. For some anatomical structures, such as the wrist joint, arm or knee, the images are obtained in projections targeting the specific anatomical structure.

X-ray diagnostics is a relatively inexpensive testing method. It provides quick diagnostic information on fractures, pathological changes in bones, dislocations, subluxations and/or soft tissue edema. Due to the ionizing radiation involved, it is very important to choose the right projection so that the diagnostic process is as effective as possible. It should be noted that the person referring the patient for testing using ionizing radiation should issue a referral including clinical information and a legitimate purpose for the testing. The patient should also be informed about the need to provide previous tests.

## **Ultrasonography**

Ultrasonography is a method that uses ultrasound to obtain cross-sections of individual tissues. The method is noninvasive, safe (it does not use ionizing radiation), relatively cheap and widely available. It is used in many clinical situations, including osteoarticular system diagnostics. Ultrasound waves, or waves with a very high frequency, are very important in musculoskeletal system diagnostics, which is why—apart from the experience of the radiologist—a good ultrasound device with a linear head working at a high frequency is of great importance.

Musculoskeletal ultrasonography allows for real-time, static and dynamic assessment of bone and joint structures. Ultrasonography is a perfect tool for assessing structural damage to muscles, tendons and nerves. Moreover, it provides the ability to examine the patient after the implantation of metallic implants when magnetic resonance imaging (MRI) cannot be performed and computed tomography would show artifacts. However, ultrasonography, like any other medical procedure, has some limitations, including primarily the incomplete penetration of body structures by

ultrasound waves. In addition, when ultrasound waves reach areas filled with gas, the waves are 100% reflected.

The main indications for ultrasonography include complaints in the following anatomical regions:

- wrist and metacarpal joints,
- elbow joint,
- shoulder joint,
- hip joint,
- knee joint,
- ankle joint,
- metatarsal joints,
- muscular structures of the whole body,
- peripheral nerves.

In addition to the organic structures of bones and joints, ultrasound diagnostics may be supplemented by Doppler ultrasound for the evaluation of blood flow in vessels. Doppler ultrasound can be used for the evaluation of soft tissue vascularization. Ultrasonography allows for fast, and cost-effective follow-up examinations.

In the case of bones and joints, ultrasound examination is good for the assessment of rotator cuff structures, e.g., in the event of injury to the supraspinatus tendon, especially in athletes practicing throwing sports. For some indications, the accuracy of ultrasound is almost comparable to that of magnetic resonance imaging (MRI).

Ultrasonography is also ideal for assessing changes in the attachments of the proximal flexor and extensor muscles of the wrist, known as "tennis elbow" and "golfer's elbow." In combination with palpation, edematous changes, their extent, exudate in the articular cavity and possible damage to muscle structures can be determined. Such a diagnosis directly translates to targeted physiotherapy in the field of therapeutic treatment and the targeted use of Kinesio Tape®, which should not be performed without knowledge of anatomy.

Ultrasound is used in not only diagnostic imaging but also therapy. It allows for direct treatment and indirect targeted drug injection within muscle and joint structures. Many years ago, it was discovered that drug administration under ultrasound guidance is more effective than so-called blind injection. Ultrasound diagnostics allows for the precise assessment of parenchymatous

organs, such as the liver, spleen, kidneys, and pancreas. Lymph nodes are also perfectly visible.

Ultrasound examination is an excellent tool in everyday, high-efficiency diagnostic practice. The method is widely available, safe and relatively cheap, but its effectiveness largely depends on the skills of the radiologist.

## **Computed tomography**

Computed tomography (CT) is an examination that yields cross-sections of the human body with the possibility of 2D or 3D image reconstruction. CT, similar to X-ray examination, uses X-rays to visualize the examined structures. CT has a wide range of applications in medicine, and it is the basic testing modality applied for trauma patients.

Native, precontrast scanning phases, as well as arterial, venous and late phases after the intravenous administration of contrast media, are applied.

CT examination is also a sensitive test for evaluation of the articular labrum of large joints after the administration of a contrast agent into the joint cavity.

## **Multislice computed tomography (MSCT)**

Currently, 64-slice to 256-slice CT systems are used. Modern CT units are equipped with two X-ray tubes for dual-energy scanning. Such solutions improve image quality and allow for CT spectroscopy to identify different tissues and contrast agent perfusion). The CT scans encompass an entire volume; therefore, it is easy to obtain multiplanar reformatted reconstruction (MPR), maximum intensity projection (MIP) and volume rendering (VR) images. The MPR method involves the reconstruction of images in any possible plane. It is commonly used to assess the musculoskeletal system and the cardiovascular system. The MIP reconstruction method is useful in the assessment of blood vessels. VR allows for the spatial imaging of each anatomical structure, e.g., fractured bones, especially for the display of displaced bone fragments.

In conclusion, CT is an excellent imaging technique in the assessment of all body structures, especially bones. Before referring a patient for CT, the doctor should always bear in mind the side effects of the use of X-rays.

## **Magnetic resonance imaging (MRI)**

MRI is an examination method that uses atomic resonance and the relaxation time of molecules in the body for imaging. MRI in medicine is used to analyze the whole body. It is widely used in the diagnosis of osteoarticular and brain pathologies.

By changing some imaging parameters, a variety of datasets can be obtained, yielding different images, including T1-weighted images, T2-weighted images, fat-suppressed images and diffusion-weighted images. Through intravenous contrast administration, perfusion tests of tissues can be performed to specify the degree of enhancement and washout of the contrast agent.

It is also possible to measure the diffusion of water molecules in tissue, which allows for the early diagnosis of stroke only minutes after its occurrence.

MRI is effective in various medical disciplines, and it is an excellent imaging method used in orthopedic surgery, neurology, oncology, cardiology, and many other areas. It is an irreplaceable tool in the diagnosis of the osteoarticular pathologies. In neuroradiology, MRI allows for the assessment of focal lesions in the brain and spinal canal, as well as vascular and posttraumatic pathologies. Basic MRI shows high specificity and sensitivity in the detection of brain pathologies.

MRI is also used in the comprehensive assessment of the osteoarticular system and is even more precise than ultrasonography. MRI is an excellent testing method for assessing the structures of the musculoskeletal system, especially hidden elements that are not visible on ultrasound, e.g., articular labrum and ligaments, such as the glenohumeral ligaments, and changes in the area of the spine or in the sacroiliac joints.

MRI perfectly images joint cartilage and is noninvasive. The selection of appropriate sequences allows for the imaging and assessment of injuries to the cartilage in the area of the joint surface.

In summary, MRI is an excellent noninvasive testing method used for the assessment of the osteoarticular system and examination of the whole body. In the case of the musculoskeletal system, it is often the method of choice for evaluating the degree of injury before a planned surgical procedure. However, while considering MRI, it should be remembered that this method is relatively expensive and time consuming.

## CHAPTER TWO

### BRAIN IMAGING

This chapter will provide basic information on the diagnostic imaging of intracranial structures by CT and MRI.

CT and MRI were introduced in the early 1970s and 1980s. From the very beginning, the application of both of these methods in neuroimaging marked a new, increasingly basic diagnostic element in the assessment of intracranial pathologies.

CT and MRI are basic methods for imaging brain tissue and are widely used in the daily work of a radiologist. CT has replaced the traditional X-ray examination. CT is a fast method that allows for the diagnosis of craniocerebral injuries, hemorrhagic changes, edema, and cerebrovascular changes and the assessment of fractures of the bone structures (Figures 2.1, 2.2).

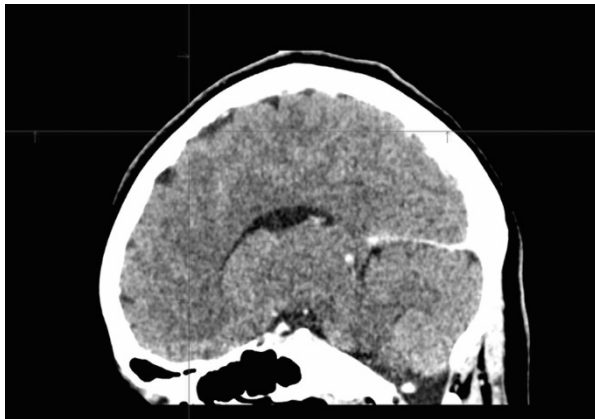


Figure 2.1. a) Normal brain on sagittal CT image.



Figure 2.1 b). Normal brain on transverse CT image after contrast application.

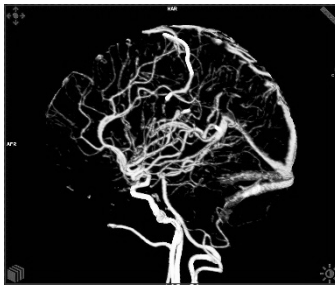


Figure 2.2. Normal brain vessels visible on angio-CT after 3D reconstruction in the sagittal plane.

## Brain injury—the basics

### Epidural hematoma

Epidural hematoma is a traumatic accumulation of blood between the skull (lamina rara interna) and the dura mater. It is often a result of a blunt force with the disruption of a meningeal arterial vessel, and in most cases, it is formed in the temporoparietal region of the head. Epidural hematoma typically demonstrates biconvex fluid accumulation on CT or MRI.

### Subdural hematoma

Subdural hematoma is the accumulation of blood in the space between the dura mater and the arachnoid mater (Figures 2.3, 2.4). Traffic accidents and beatings are the most common reasons for this type of injury.



Figure 2.3. Chronic subdural hematoma after road accident visible on transverse CT image.

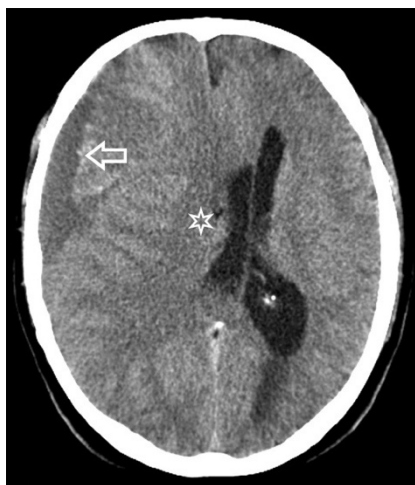


Figure 2.4. Subdural hematoma (arrow) with mass effect visible on CT in the transverse plane (asterisk). Parts of the hematoma is hypodense indicating also old hemorrhage.

### Subarachnoid hemorrhage

A subarachnoid hemorrhage is the accumulation of blood in the subarachnoid area between the arachnoid mater and the pia mater (Figure 2.5). The assessment of hemorrhagic changes by CT without contrast is used to determine the location of blood and its metabolites.



Figure 2.5. Subarachnoid hemorrhage due to a ruptured aneurysm (arrow), blood also entered into the lateral ventricle (asterisk).

### Cerebrovascular incidents

Cerebrovascular incidents may be classified as ischemic or hemorrhagic. Depending on the type of stroke, patients may experience a sudden onset of focal neurological deficit, various degrees of paralysis, visual field defects, lack of movement and coordination, dizziness, aphasia or loss of consciousness. Up to 85% of all vascular incidents are related to ischemia caused by embolism or thrombosis with partial or total occlusion of the vessel lumen (Figures 2.6, 2.7).

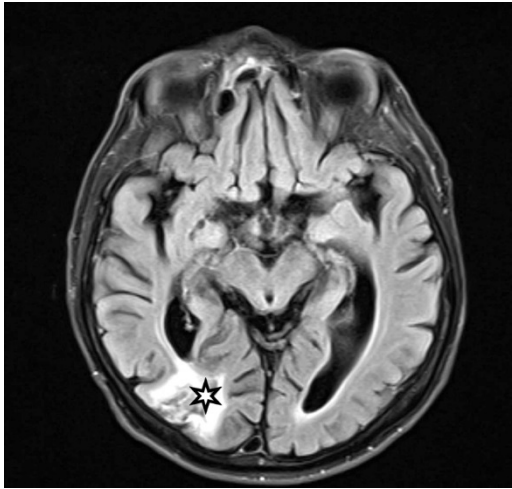
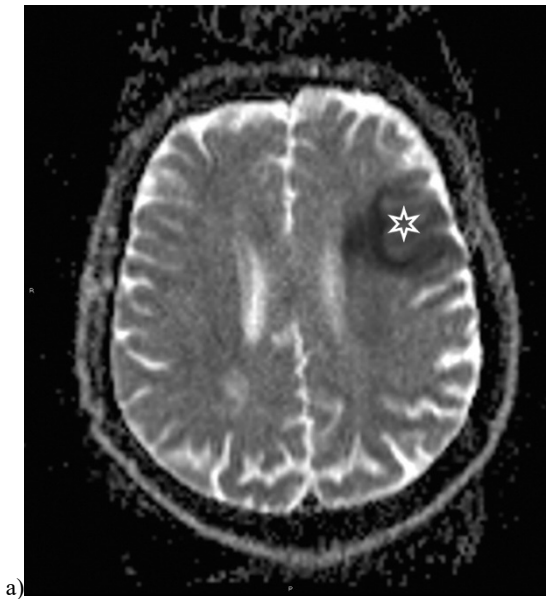


Figure 2.6. Ischemic changes in the subacute phase in the right occipital lobe (asterisk) observed on MRI with the FLAIR sequence in the transverse plane.



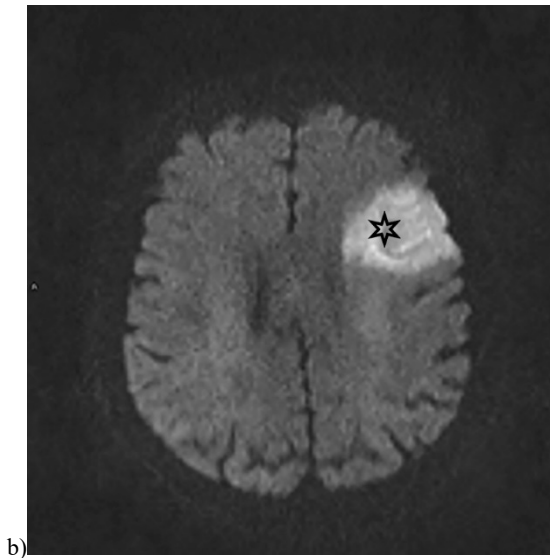


Figure 2.7. Acute stroke visible on transverse MR image in a) ADC and b) DWI. DWI and ADC sequence reveals diffusion restriction in ischemic lesion (asterisk), left side which is typical for acute phase of the disease.

## Vascular changes

One of the basic applications of CT and MRI is imaging blood vessels to exclude intracerebral changes of a vascular malformation character. The evaluation of blood vessels can be carried out using CT or MRI sequences with or without the intravenous administration of a contrast agent. The assessment of vessels by both MRI and CT is carried out through multidimensional analysis and 3D reconstruction. CT and MRI can reveal vascular changes or their absence at the capillary level, e.g., CT or MRI perfusion (Figures 2.8–2.10).

Perfusion parameters, i.e., cerebral blood flow, cerebral blood volume and the average blood transit time, are determined quantitatively. Such an analysis allows the assessment of the extent of stroke-related ischemic lesions.

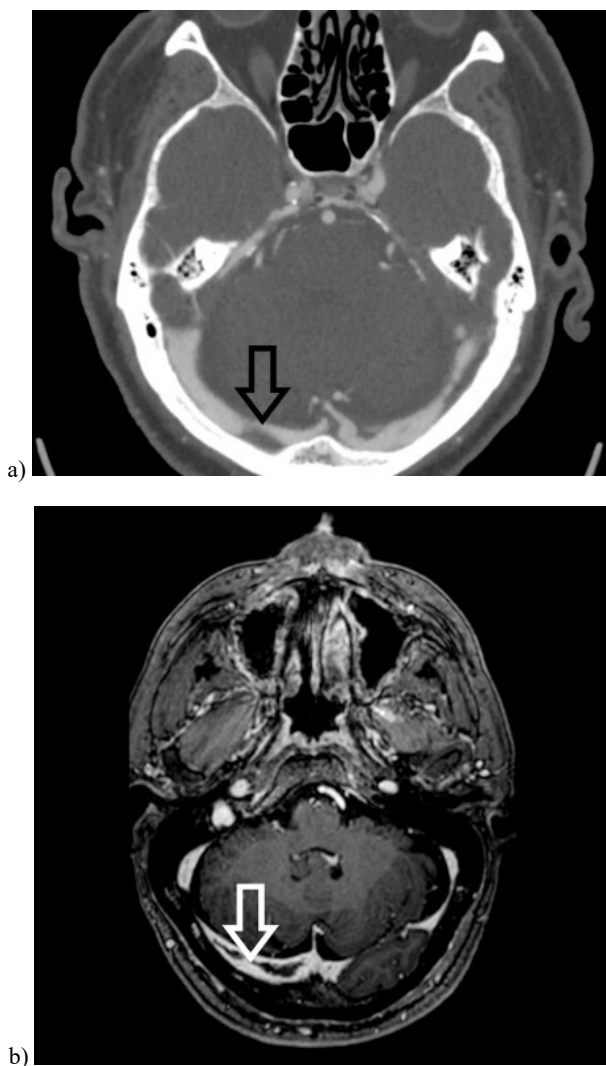


Figure 2.8. Transverse sinus thrombosis: a) thrombosis on the right side visible on transverse CT image (black arrow); b) thrombus on the right side visible on MRI with the T1-weighted sequence in the transverse plane after the intravenous administration of a contrast agent (white arrow).